RMetS
Royal Meteorological Society

Composite hodographs and inertial oscillations in the nocturnal boundary layer

P. Baas,[a]* B. J. H. van de Wiel,[b] L. van den Brink[c] and A.A.M. Holtslag[c]

[a]*Royal Netherlands Meteorological Institute, De Bilt, The Netherlands*
[b]*Vortex Dynamics, Department of Applied Physics, Eindhoven Technical University, The Netherlands*
[c]*Meteorology and Air Quality, Wageningen University and Research Centre, The Netherlands*

*Correspondence to: P. Baas, KNMI, Regional Climate, Wilhelminalaan 10, De Bilt, 3730AE, Netherlands.
E-mail: baasp@knmi.nl

In this work the dynamic behaviour of the wind in the nocturnal boundary layer is studied, with a particular focus on systematic behaviour of the near-surface wind. Recently, an extension of the well-known Blackadar model for frictionless inertial oscillations above the nocturnal boundary layer was proposed by Van de Wiel *et al.*, which accounts for frictional effects within the nocturnal boundary layer. It appears that the nocturnal wind velocity profile tends to perform an inertial oscillation around an equilibrium wind profile, rather than around the geostrophic wind vector (as in the Blackadar model).

In the present study we propose the concept of 'composite hodographs' to evaluate the ideas and assumptions of the aforementioned analytical model. Composite hodographs are constructed based on a large observational dataset from the Cabauw observatory. For comparison and deeper analysis, this method is also applied to single-column model simulations that represent the same dataset. From this, it is shown that winds in the middle and upper part of the nocturnal boundary layer closely follow the dynamics predicted by the model by Van de Wiel *et al.* In contrast, the near-surface wind shows more complex behaviour that can be described by two different stages: (1) a decelerating phase where the wind decreases rapidly in magnitude due to enlarged stress divergence in the transition period near sunset (an aspect not included in the analytical model), and (2) a regular type of inertial oscillation, but with relatively small amplitude as compared to the oscillations in the middle and upper parts of the nocturnal boundary layer. Copyright © 2011 Royal Meteorological Society

Key Words: low-level jets; stable boundary layer; single-column modelling; near-surface wind; composite observations

Received 21 February 2011; Revised 17 August 2011; Accepted 2 September 2011; Published online in Wiley Online Library

Citation: Baas P, van de Wiel BJH, van den Brink L, Holtslag AAM. 2011. Composite hodographs and inertial oscillations in the nocturnal boundary layer. *Q. J. R. Meteorol. Soc.* DOI:10.1002/qj.941

1. Introduction

Inertial oscillations (IOs) are a well-known phenomenon in boundary-layer meteorology. These oscillations in the wind typically occur during night-time as a result of the sudden collapse of convective turbulence near sunset (e.g. Stull, 1988). In particular, IOs occurring above the nocturnal inversion layer that manifest themselves in the appearance of the so-called nocturnal low-level jet (LLJ) have been studied intensively (Bonner, 1968; Garratt, 1985; Kraus *et al.*, 1985; Smedmann *et al.*, 1993; Beyrich, 1994; Whiteman *et al.*, 1997; Wilczak *et al.*, 1997; Andreas *et al.*, 2000; Song *et al.*, 2005; Baas *et al.*, 2009; among others). We note that LLJs are not generated by IOs alone, as many dynamical forcing mechanisms may trigger their formation (Holton, 1967; Kotroni and Lagouvardos, 1993; Stensrud, 1996; Banta

et al., 2002; Lundquist, 2003; Jiang *et al.*, 2007, Shapiro and Fedorovich, 2009).

In contrast to these high-level IOs, their appearance *within* the nocturnal boundary layer (NBL) has received much less attention. An important reason for this is the fact that IOs at lower levels are usually less clearly visible in observations, as their amplitude is reduced by surface friction. Furthermore, in the vicinity of the surface the wind is prone to local effects, which complicates its behaviour. In the current study we present a method to circumvent these issues, which allows us to focus on those lower-level IOs.

One of the simplest and most well-known concepts for understanding IOs in the atmospheric boundary layer is the model of Blackadar (1957, henceforth B57), which has become standard in boundary-layer meteorology. According to B57, the rapid collapse of convective turbulence near sunset causes an imbalance in the local momentum budget. As a consequence, above the inversion layer the wind vector performs a frictionless, undamped oscillation around the geostrophic wind with a period of $2\pi/f$ (where f is the Coriolis parameter) and an amplitude equal to the initial ageostrophic wind speed. Though the B57 theory explains the appearance of IOs above the inversion layer, it is clearly not applicable within the NBL, where frictional effects are non-negligible. Buajitti and Blackadar (1957) extended the B57 model to include the effects of surface friction. Following these pioneering studies, numerous conceptual and analytical models have been developed to improve the understanding of IOs in the atmospheric boundary layer (Thorpe and Guymer, 1977; Beyrich and Klose, 1988; Singh *et al.*, 1993; Tan and Farahani, 1998; Shapiro and Fedorovich, 2010). Although these studies clearly improved the understanding of the diurnal dynamics of the wind profile, their approach is usually rather complex.

Recently, Van de Wiel *et al.*(2010, henceforth VdW10) formulated a generalization of the B57 model to include the effects of surface friction, while, at the same time, leaving the structure and simplicity of this model intact (see section 2). According to the VdW10 model, the nocturnal wind profile does not describe an inertial oscillation around the geostrophic wind vector, but rather an oscillation around the equilibrium wind profile (which makes B57 a special case for a frictionless equilibrium). Thus, this model extends the validity of the B57 model, being applicable above and within the NBL. Because, for each height, the model predicts hodographs with a characteristic shape resembling horseshoes, in this study we simply refer to this model as the 'horseshoe model'.

In VdW10 a qualitative comparison of the model with observations from the Cabauw observatory (The Netherlands) gave reasonable agreement. On the other hand, it is clear that the model's assumptions may have limitations, especially around sunset when the boundary layer has a highly transient character. To enable a more robust evaluation of the concepts and assumptions of the horseshoe model, in the present study we investigate the behaviour of the NBL winds in more depth, by applying a new method which uses so-called 'composite hodographs'. With this methodology it is possible to construct a generic hodograph which is an average over many individual hodographs of different nights with different geostrophic forcing characteristics. In this way, particular disturbances (e.g. subtle variations in the geostrophic wind or in the momentum advection) that may obscure the shape of individual hodographs (especially at lower levels) are largely averaged out, such that the more general structure of the NBL winds can be determined from the observations. Composite hodographs (CHs) will be constructed for selected cases from the Cabauw observatory. For comparison and a more in-depth analysis, the same methodology is applied to results of a state-of-the-art single-column model.

2. The 'horseshoe' model

For convenience, in this section we briefly summarize the model introduced by VdW10. The points of departure are the boundary-layer equations for the mean components of the horizontal wind, U and V (we omit the overbar for mean variables):

$$\frac{\partial U}{\partial t} = fV + \frac{\partial \tau_x/\rho}{\partial z}, \tag{1}$$

$$\frac{\partial V}{\partial t} = f(G - U) + \frac{\partial \tau_y/\rho}{\partial z}, \tag{2}$$

where τ_x and τ_y represent the horizontal turbulent stresses, ρ the density of air, and f the Coriolis parameter. For both equations, the term at the l.h.s. represents the acceleration term, the terms at the r.h.s. represent the Coriolis term (consisting of the sum of the usual Coriolis term and the pressure gradient term) and the stress-divergence term, respectively (note that we consider the advection terms equal to zero). The coordinate system is chosen such that the x-axis is aligned with the geostrophic wind vector (with magnitude G). In the B57 approach it is assumed that friction disappears above the inversion layer at the onset of the NBL. As such, the stress-divergence terms, which represent the boundary-layer friction, become zero. By assuming an initial profile at the onset of the inertial oscillation, $U = U_0$, $V = V_0$ at $t = 0$, the time-evolution of U and V becomes:

$$U - G = (V_0 - 0)\sin(f\,t) + (U_0 - G)\cos(f\,t), \tag{3}$$

$$V - 0 = (V_0 - 0)\cos(f\,t) - (U_0 - G)\sin(f\,t). \tag{4}$$

The reason for writing the solution in this form becomes clear below. Note that the frictionless equilibrium solution of Eqs (1) and (2) is: $U_{\mathrm{eq}} = G$, $V_{\mathrm{eq}} = 0$, so that Eqs (3) and (4) represent oscillations around this equilibrium. For each height, the amplitude of the oscillation equals the initial ageostrophic wind speed.

Alternatively, the following equilibrium solution of Eqs (1) and (2) is considered:

$$\frac{\partial \tau_{x,\mathrm{eq}}/\rho}{\partial z} = -fV_{\mathrm{eq}}, \tag{5}$$

$$\frac{\partial \tau_{y,\mathrm{eq}}/\rho}{\partial z} = -f(G - U_{\mathrm{eq}}). \tag{6}$$

Since we do not invoke a specific eddy viscosity closure (as for example Monin–Obukhov similarity theory), this is a nonconventional turbulence closure assumption. Next, rather than ignoring the stress-divergence terms in Eqs (1) and (2), we approximate these by the equilibrium expressions Eqs (5) and (6). In other words: it is assumed that the *actual friction* during and after the evening transition *equals* the friction that would be present in the *equilibrium nocturnal boundary layer*. Under this assumption, friction

becomes time-independent and a function of height only. By replacing the last terms of (1) and (2) by (5) and (6) we obtain:

$$\frac{\partial(U-U_{\rm eq})}{\partial t} = f(V-V_{\rm eq}), \tag{7}$$

$$\frac{\partial(V-V_{\rm eq})}{\partial t} = -f(U-U_{\rm eq}). \tag{8}$$

Note that the components $U_{\rm eq}$ and $V_{\rm eq}$ can be included within the differential operators since $\partial U_{\rm eq}/\partial t = \partial V_{\rm eq}/\partial t = 0$. Consequently, the equations are expressed in '*departure-from-equilibrium*' form rather than in terms of geostrophic departure. The solution of Eqs (7) and (8) reads:

$$U - U_{\rm eq} = (V_0 - V_{\rm eq})\sin(f\,t) + (U_0 - U_{\rm eq})\cos(f\,t), \tag{9}$$

$$V - V_{\rm eq} = (V_0 - V_{\rm eq})\cos(f\,t) - (U_0 - U_{\rm eq})\sin(f\,t). \tag{10}$$

However, assumptions have to be made regarding $U_{\rm eq}$ and $V_{\rm eq}$, which, for example, can be based on Ekman solutions of the boundary-layer equations (see VdW10 for an extensive discussion). Initial profiles, on the other hand, can be specified freely (e.g. from observations). Obviously, the solution depends on both the choice of the equilibrium profiles and the initial profiles. It is clear that the B57 solutions (Eqs (3) and (4)) now become a special case of Eqs (9) and (10).

To illustrate the implications of Eqs (9) and (10), Figure 1 shows hodographs (nocturnal part) for three different levels for a case observed at the Cabauw observatory (see section 3.2). At this location the inertial period amounts to 15.2 h. Since this is longer than the length of the night, the hodographs in the Figure are not closed. The ends of the initial velocity vectors are indicated by grey triangles. To compare the observations with the model, equilibrium wind vectors are needed. For the purpose of illustration, we simply assume that at each level the equilibrium vector is reasonably represented by the vector-averaged observations (indicated by the black dots). This is a rather crude assumption (which, for example, assumes stationary external forcings), but it may help to obtain a qualitative understanding of IO dynamics (see VdW10 for a more thorough discussion).

Since at the time of the initialization the boundary layer is still well-mixed, both the magnitude and the direction of the initial wind vectors are relatively uniform as compared to the night-time equilibrium vectors for those levels. According to the model, the wind vectors perform a clockwise rotation around equilibrium (Northern Hemisphere). As a result of the well-mixed character of the initial profile, the initial wind speed at 200 m is lower than the nocturnal equilibrium vector, while at 10 m the initial wind speed is higher than its equilibrium value. For the higher level this implies a classical IO with an initial increasing wind vector magnitude. In contrast, clockwise rotation at the near-surface level implies an initial decrease of the magnitude of the wind vector. At the middle level, the wind vector forms a compromise between the extremes, as the orientation of the 'horseshoe' changes systematically with height.

For this specific case, both model and observations show reasonably similar IOs. However, from just a single case it is not obvious that the model should have general validity. Therefore, to assess the merits and shortcomings of the horseshoe model, in the present study we analyse a large set of observations together with numerical model integrations.

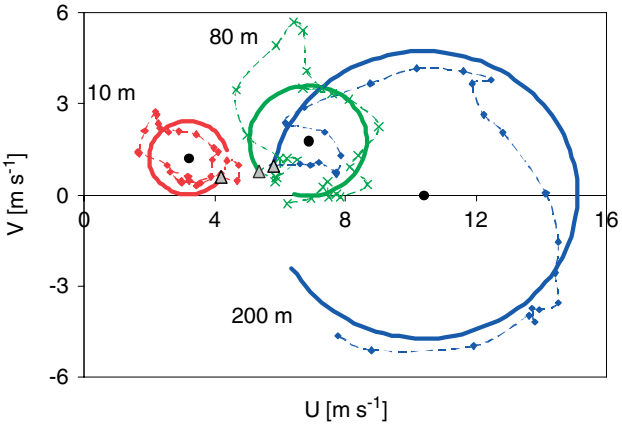

Figure 1. Hodographs for three different levels observed at the Cabauw observatory (15–16 July 2006). Observations are given by the thin dashed lines (each symbol represents a half-hour value), whereas results by the analytical model are given in thick lines. Grey triangles indicate the initial wind vectors and the black dots correspond to the (supposed) equilibrium vectors (see text). This figure has been adopted from Van de Wiel *et al.* (2010). This figure is available in colour online at wileyonlinelibrary.com/journal/qj

3. Method

3.1. Composite hodographs

To enable a robust evaluation of the analytical model described above, we introduce the concept of composite hodographs (CHs) (Van den Brink, 2010). As explained below, by re-orientating and normalizing hodographs of individual cases, averaged hodographs are constructed. Composite observations provide a better picture of generic characteristics than can be obtained from studying mere individual cases, which are often disturbed by all kinds of dynamic disturbances of various scales (e.g. meandering of the flow, wave activity, mesoscale circulations, changes at the synoptic scale). The concept of averaged hodographs was used earlier by, for example, Buajitti and Blackadar (1957), but they did not utilize a normalization procedure.

To construct a CH, first, hodographs of selected individual cases are rotated into the direction of the vector-averaged geostrophic wind ($V_{\rm g}$) which is estimated from surface pressure observations (see section 3.2). Since our study focuses on the NBL, we take the average between 1800 UTC and 0600 UTC as a reference. When reliable estimates of $V_{\rm g}$ are lacking, wind observations could be used as a proxy, although this may impact the final orientation of the CHs. If we use observations from the 200 m level, we obtain nearly identical results, since at this level the average wind direction between 1800 and 0600 UTC is close to the average direction of $V_{\rm g}$.

Second, for each case the rotated hodographs are normalized with the corresponding magnitude of the geostrophic wind. This normalization enables averaging of nights with different forcing conditions. Formally, one should also normalize the CHs with respect to a typical depth scale, such as the depth of the Ekman layer or the LLJ height (cf. Banta *et al.*, 2006). However, since in our case the variations of the LLJ height (mostly around 200 m) are rather small compared to the vertical resolution of the observations, we considered this impractical.

Finally, for each level the re-orientated and normalized hodographs are averaged to yield a set of CHs.

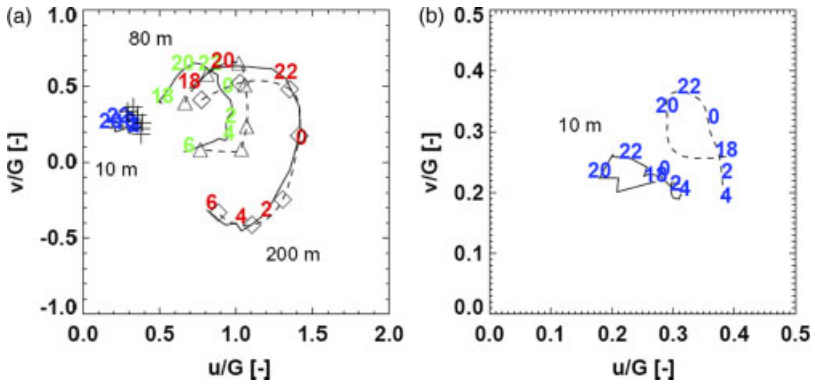

Figure 2. (a) Composite hodographs over eight nights between 1800 and 0600 UTC for 10, 80 and 200 m above the surface. (b) Composite hodographs for the 10 m level, magnified. The dashed lines represent the SCM results; the numbers indicate hours in UTC. For clarity, in (a) time indicators for the SCM results have been replaced by symbols (10 m plus signs; 80 m triangles; 200 m diamonds). This figure is available in colour online at wileyonlinelibrary.com/journal/qj

3.2. *Observations and case selection*

We investigate a composite case constructed from wind observations obtained from the Cabauw measurement site (The Netherlands). The observatory is situated in topographically flat and relatively open terrain (51.971°N, 4.927°E). Detailed characteristics can be found in Van Ulden and Wieringa (1986) and Beljaars and Bosveld (1997). In this study we utilize observations from the 213 m high main tower. Wind measurements are taken with cup anemometers at six levels (10, 20, 40, 80, 140 and 200 m).

To obtain suitable cases for the composite case, we examined 10 years of continuous observations (2001–2010). We focus on the months May, June and July, because in this period the night-time length is relatively constant. The main forcing factors of the NBL are the geostrophic wind speed and the (isothermal) net (long-wave) radiation (Van de Wiel *et al.*, 2003). Earlier research at Cabauw has demonstrated that the most significant LLJs occur for moderately strong geostrophic wind speeds combined with a strong radiative cooling (Baas *et al.*, 2009). Therefore, following a similar procedure as in Baas *et al.*(2010), for the 10 years of observations we selected all 24 h periods (1200–1200 UTC; local solar time is 20 minutes ahead of UTC) with practically clear-sky conditions and a moderately strong geostrophic wind; the magnitude of the net long-wave radiative cooling was required to be above 20 W m^{-2} over the full 24 h period, while between 1800 and 0600 UTC the geostrophic wind speed was continuously between 5 and 15 m s^{-1} with less than 3 m s^{-1} variation. The geostrophic wind was derived from a planar fit of surface pressure observations obtained from eight synoptic weather stations in a radius of 75 km around Cabauw. (Since only surface estimates of the geostrophic wind were available, height-dependent variations of the geostrophic wind associated with the thermal wind were not accounted for.)

From the 10 years of observations, 28 nights satisfied the above criteria. By visual inspection of the 200 m hodographs a subset of eight cases was composed to simulate with a single-column model (SCM). Since large-scale forcings are a major source of uncertainty in SCM integrations, only these cases were selected which exhibited a strong and 'ideally' developing IO. We assume that in these cases the influence of disturbances is relatively small.

3.3. *Single-column model*

To study the behaviour of the wind in the NBL in more detail we made SCM integrations for the subset of eight selected cases using the single-column model (SCM) version of the Integrated Forecasting System (IFS) of the European Centre for Medium-range Weather Forecasting (ECMWF), CY31r1. The model physics are extensively described at http://www.ecmwf.int/research/ifsdocs/CY31r1/index.html. The SCM is run in full interaction with a soil/vegetation scheme. Radiative fluxes are accounted for by a radiative transfer model.

We used a modified version of the model, in which the standard first-order vertical diffusion scheme was replaced by a turbulent kinetic energy (TKE) closure formulation, which is described in detail by Lenderink and Holtslag (2004). The parameters in the turbulence scheme are chosen in such a way that the model's mixing characteristics resemble the values obtained from field experiments.

The large-scale forcings (i.e. the components of the geostrophic wind, vertical velocity, and the horizontal dynamical tendencies of momentum, temperature and humidity) needed to drive the SCM were derived from short-range forecasts by a numerical weather prediction (NWP) model, in this case the Regional Atmospheric Climate Model (RACMO2) (Van Meijgaard *et al.*, 2008). This model uses the semi-Lagrangian dynamics kernel of the High Resolution Limited-Area Model (HIRLAM), while the physical package is derived from the ECMWF model. The NWP runs were initialized by the global ECMWF analysis. In the SCM, the vertical advection is calculated from the vertical velocity as provided by the RACMO2 runs and the vertical gradients as calculated by the SCM itself. Initial profiles were directly taken from the NWP simulations. No data assimilation has been applied in either the SCM or RACMO2. Both models are initialized at the same time.

The SCM experiments have been configured as follows. The simulations are initialized at 1200 UTC; the integration time is 24 h. The model contains 80 vertical levels. The lowest model levels are situated at approximately 10, 30, 60, 90, 125, 170, 210 and 270 m above the surface. The time step is 10 minutes. For each simulation the results were interpolated towards the levels of the tower observations. Next, CHs were constructed as described in section 3.1.

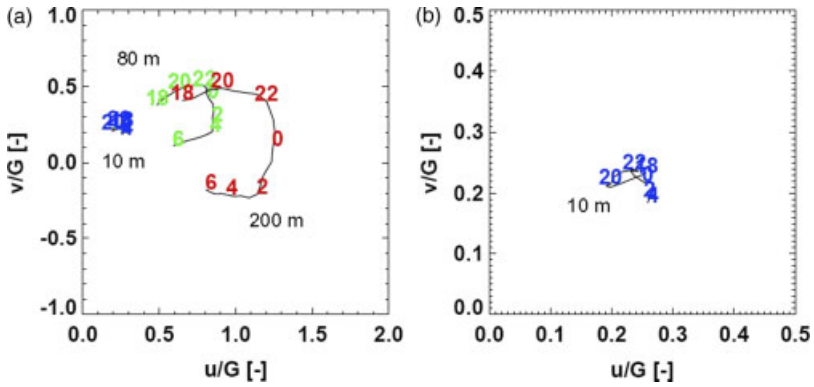

Figure 3. (a) Composite hodographs over 28 nights between 1800 and 0600 UTC for 10, 80 and 200 m above the surface. (b) Composite hodograph for the 10 m level, magnified. The numbers indicate hours in UTC. This figure is available in colour online at wileyonlinelibrary.com/journal/qj

4. Results

4.1. Composite hodographs of observations and single-column model results

Figure 2 presents CHs for the subset of eight cases that were selected in the previous section. First, we focus on the observations. At 200 m the wind vector rotates smoothly around the geostrophic wind, resembling the classical forward IO, which has been documented so well in literature. In the middle section of the NBL, at 80 m, the wind vector still undergoes a significant oscillation. However, the centre of rotation is no longer the geostrophic wind and the amplitude is reduced. Apparently, at the intermediate levels the wind vector rotates around an equilibrium wind vector, as suggested by the analytical model of VdW10.

Contrary to the wind in the intermediate and upper parts of the NBL, the behaviour of the wind vector close to the surface is more complex, and can be split into two separate phases:

(1) Phase I: a strong decrease of the magnitude of the wind vector. As will be show later, this decrease is primarily caused be a period of enhanced stress divergence during the evening transition. The horseshoe model cannot reproduce this phase.
(2) Phase II: the wind vector seems to rotate around some equilibrium wind vector. The amplitude is small. In section 4.2 we explore the behaviour of the near-surface wind vector in more detail.

The correspondence between CHs obtained from the SCM results and observed CHs is remarkable (Figure 2), especially at the intermediate and higher level (80 and 200 m). Also, the shape of the 10 m hodograph is rather similar, in view of the low-level wind complexity. Given the ability of the model to reproduce the observed CHs, we are confident to use the SCM to study the dynamics of the inertial oscillations in more detail (see section 4.2).

It can be argued that by selecting only cases with strong and ideally behaving IOs, our composite case is somewhat tailored towards the 'desired' behaviour. Therefore, we have also constructed CHs for our initial selection of 28 nights, which were selected on objective criteria only, i.e. the geostrophic wind and the net long-wave radiation. Figure 3 presents CHs for 10, 80 and 200 m above the surface. The correspondence with Figure 2 is striking. This confirms the results of the pre-selected cases given above, suggesting that the observed behaviour has a more general validity (at least for the present site) for clear-sky nights with moderate geostrophic forcing conditions.

The results for the two upper levels are very robust with respect to the exact selection criteria. Conversely, the CH of the 10 m wind is sensitive to the threshold values of net long-wave radiation and geostrophic wind, which illustrates the complexity of the near-surface wind behaviour (cf. Van den Brink, 2010). For example, entirely omitting the selection criteria on geostrophic wind and applying the same criteria for the net long-wave radiation (yielding 190 nights over the period considered) leaves the CHs at 80 and 200 m largely unchanged, while the 10 m hodograph shows a more diffuse behaviour.

4.2. Idealized case

As has been demonstrated above, the dynamics of the near-surface wind is more complex than the horseshoe model assumes. To augment the understanding of the near-surface wind behaviour, in this section we set up an idealized SCM experiment, with constant geostrophic wind and no advective tendencies. Such ideal cases are difficult to extract from real observational cases, since these are often affected by a variety of dynamic disturbances of various scales.

Figure 4 shows hodographs (scaled by the geostrophic wind) composed of results from the idealized SCM integration. During the afternoon the wind vectors of the different levels are close together as a result of efficient momentum mixing. At 1810 UTC the surface sensible heat flux becomes negative and a growing NBL starts to develop (note that this is two hours before sunset). Convective mixing ceases and the wind vectors diverge, which increases the (directional) shear. During the night, the upper levels follow a well-defined inertial oscillation around an equilibrium wind vector. An Ekman profile with an assumed eddy diffusivity of 0.22 $m^2\ s^{-1}$ seems to provide a fair representation of the equilibrium profile. Note that such representation has little validity near the surface where the assumption of 'constant eddy diffusivity' is clearly unrealistic.

At 10 and 40 m above ground level the situation is clearly different. As described above, two stages can be indentified. At both levels, in the first hour after decoupling, the wind speed drops quickly (Phase I). Next, the wind vectors start rotating around some equilibrium (Phase II). Although the amplitude is gradually reduced when approaching the

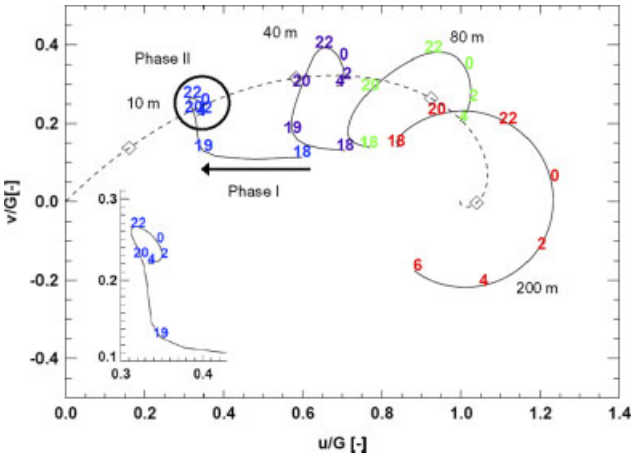

Figure 4. Hodographs at 10, 40, 80, and 200 m above the surface from an SCM experiment with idealized forcings. The dashed line represents an Ekman spiral with an eddy-diffusivity of 0.22 m^2 s^{-1}; symbols indicate the heights of the respective hodographs. For clarity, the inset presents an enlargement of the 10 m level. Phase I and Phase II are discussed in the text. This figure is available in colour online at wileyonlinelibrary.com/journal/qj

surface, the conceptual notion that at all levels in the NBL the wind vector rotates around an equilibrium wind seems to hold.

As a next step, Figure 5 presents an analysis of the momentum budget for 10 and 200 m above the surface as obtained from the idealized SCM integration. Since in this case large-scale advection is absent, the total wind tendency is solely determined by the sum of the vertical flux divergence term and the Coriolis term. The (simplified) budget equations for momentum are given in Eqs (1) and (2).

A key assumption of the horseshoe model is the stress-divergence closure, which is assumed to be time-independent. During the transition phase this assumption will not hold. For example, the decay of convective turbulence at the end of the afternoon will invoke rapid changes in the stress divergence. This is demonstrated in Figure 5(a): shortly after the surface sensible heat flux becomes negative, the magnitude of the divergence term increases rapidly, causing a sharp drop in U (Phase I). The sequence of corresponding momentum flux profiles shown in Figure 6 explains the marked peak in the zonal flux divergence. Towards the end of the afternoon the momentum flux decreases gradually at all levels, leaving the flux divergence unchanged. As convective activity rapidly breaks down, the downward momentum transport to lower levels is greatly reduced, whereas surface friction is still relatively high because the near-surface wind speed is rather large. After a short period of time, the near-surface flux has decreased to such a level, that the flux divergence returns to pre-transition values.

The rapid decrease in U causes an imbalance in the meridional momentum budget (Eq. (2)); Figure 5(b) shows that during the transition the Coriolis term becomes larger, which induces an acceleration in V. In the remainder of the night (Phase II) the flux divergence terms are approximately constant in time. As such, in Phase II the key assumption of the horseshoe model seems to apply again.

For comparison, Figure 5(c) and (d) present the momentum budgets at 200 m above the surface. Around the evening transition the divergence terms rapidly decreases to zero. At this level the evolution of the nocturnal wind vector is completely determined by the Coriolis term.

5. Discussion

It is interesting to compare the concepts of the horseshoe model with the two-layer bulk model by Thorpe and Guymer (1977). In contrast to the former, the latter allows for a fully *time-dependent* stress parametrization. Consequently, for the near-surface layer Thorpe and Guymer (1977) obtain qualitatively good results during the transition period (e.g. their Fig. 3). However, due to its bulk nature their model is lacking height-resolving capability.

Conversely, the horseshoe model by VdW10 is fully *height-dependent*. As a result, it provides not only continuous profiles with height, but also realistic information on the gradual change of the magnitude and the orientation of the hodographs with height. However, because it assumes a time-independent stress parametrization, it is not applicable during the transition phase in the vicinity of the surface.

Though we found strong agreement between single-column model results and observations, this type of model still relies on parametrizations. To what extent these are valid in the non-stationary conditions of the transition is not yet clear. Therefore, a more physical model of turbulence like a large-eddy simulation may provide further understanding of the subtle dynamics of the wind in the developing NBL (for example, Beare *et al.*, 2006).

Finally, although we have demonstrated that the behaviour shown is quite robust for Cabauw, a similar analysis for other sites may provide additional insights into the generality of the results.

6. Conclusions

By introducing the concept of composite hodographs we are able to make a robust evaluation of the analytical model proposed by Van de Wiel *et al.*(2010), in this study denoted as the 'horseshoe model'. Re-orientating and normalizing observations allowed us to construct averaged hodographs. For a composite of selected nights from the Cabauw archive, we demonstrated that the wind vector within the nocturnal boundary layer describes an inertial oscillation around an equilibrium wind profile, rather than around the geostrophic wind. This is in line with the central assumption of the horseshoe model.

However, close to the surface the situation is more complex and here the validity of this simple analytical model is limited. The collapse of convective turbulence during the evening transition is a highly non-stationary process, for which the model is not suitable. Moreover, near the surface the wind is prone to local effects and, although we found evidence for a universal behaviour, there is a large case-to-case variability. Integrations with a single-column model proved helpful in studying the dynamics of the 10 m wind in more detail.

Analysis of the momentum budget revealed two phases in the development of the near-surface wind vector:

(1) Phase I: A strong decrease of the magnitude of the wind vector. This decrease is primarily caused by a period of enhanced stress divergence during the evening transition. As convective activity rapidly breaks down, the downward momentum transport to lower levels is reduced, whereas the surface friction is still relatively high because the near-surface wind speed is still rather large. In this phase the horseshoe model cannot be applied.

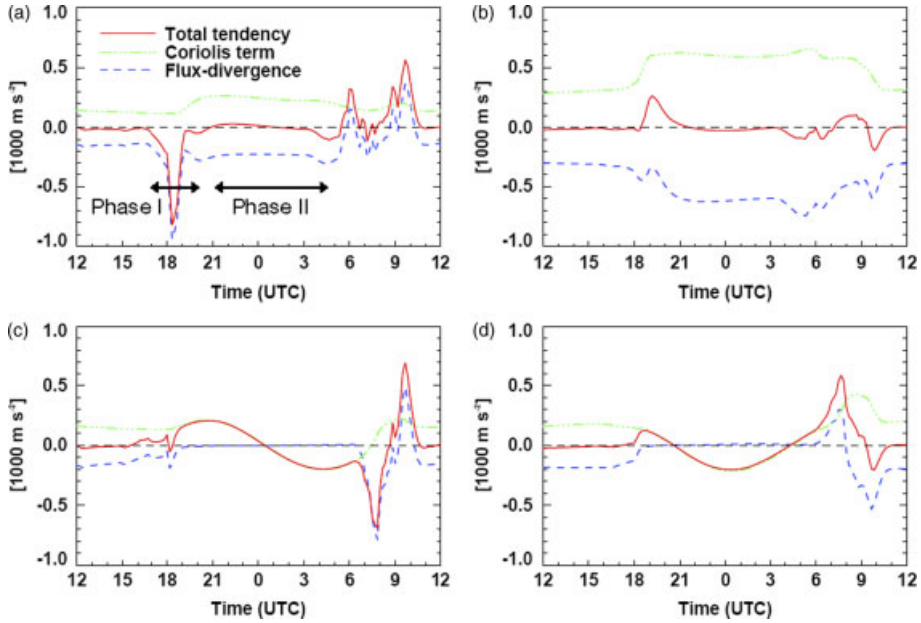

Figure 5. Time series of the various terms of the momentum budget. (a) Zonal momentum budget at 10 m. (b) Meridional momentum budget at 10 m. (c) Zonal momentum budget at 200 m. (d) Meridional momentum budget at 200 m. The phases indicated in (a) are discussed in the text. This figure is available in colour online at wileyonlinelibrary.com/journal/qj

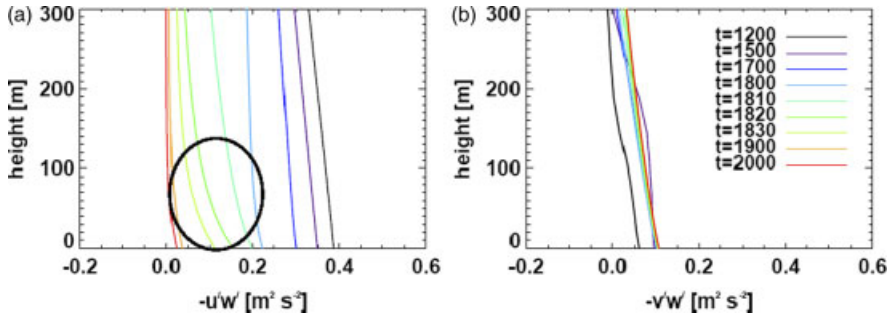

Figure 6. Profiles of the (a) zonal and (b) meridional momentum flux for selected moments in time. The oval denotes the region of enhanced flux divergence during the transition. Note that the time intervals are not constant. This figure is available in colour online at wileyonlinelibrary.com/journal/qj

(2) Phase II: A small-amplitude inertial oscillation around the equilibrium wind vector.

Acknowledgements

We thank two anonymous reviewers for their constructive comments. Fred Bosveld (KNMI) is acknowledged for providing estimates of the geostrophic wind. The first author has been supported by the US Department of Energy Earth System Modeling programme, in particular through the 'Fast Physics System Testbed and Research' (FASTER) project.

References

Andreas EL, Claffy KJ, Makshtas AP. 2000. Low-level atmospheric jets and inversions over the western Weddell Sea. *Boundary-Layer Meteorol.* **97**: 459–486.

Baas P, Bosveld FC, Klein Baltink H, Holtslag AAM. 2009. A climatology of nocturnal low-level jets at Cabauw. *J. Appl. Meteorol. Clim.* **48**: 1627–1642.

Baas P, Bosveld FC, Lenderink G, Van Meijgaard E, Holtslag AAM. 2010. How to design single-column model experiments for comparison with observed nocturnal low-level jets. *Q. J. R. Meteorol. Soc.* **136**: 671–684.

Banta RM, Newsom RK, Lundquist JK, Pichugina YL, Coulter RL, Mahrt L. 2002. Nocturnal low-level jet characteristics over Kansas during CASES-99. *Boundary-Layer Meteorol.* **105**: 221–252.

Banta RM, Pichugina YL, Brewer WA. 2006. Turbulent velocity-variance profiles in the stable boundary layer generated by a nocturnal low-level jet. *J. Atmos. Sci.* **63**: 2700–2719.

Beare RJ, Edwards JM, Lapworth AJ. 2006. Simulation of the observed evening transition and nocturnal boundary layers: Large-eddy simulation. *Q. J. R. Meteorol. Soc.* **132**: 81–99.

Beljaars ACM, Bosveld FC. 1997. Cabauw data for the validation of land surface parameterization schemes. *J. Climate* **10**: 1172–1193.

Beyrich F. 1994. Sodar observations of the stable boundary layer height in relation to the nocturnal low-level jet. *Meteorol. Z.* **3**: 29–34.

Beyrich F, Klose B. 1988. Some aspects of modelling low-level jets. *Boundary-Layer Meteorol.* **43**: 1–14.

Blackadar AK. 1957. Boundary layer wind maxima and their significance for the growth of nocturnal inversions. *Bull. Am. Meteorol. Soc.* **38**: 283–290.

Bonner WD. 1968. Climatology of the low level jet. *Mon. Weather Rev.* **96**: 833–850.

Buajitti K, Blackadar AK. 1957. Theoretical studies of diurnal wind-structure variations in the planetary boundary layer. *Q. J. R. Meteorol. Soc.* **83**: 486–500.

Garratt JR. 1985. The inland boundary layer at low latitudes. I: The nocturnal jet. *Boundary-Layer Meteorol.* **32**: 307–327.

Holton JR. 1967. The diurnal boundary layer wind oscillation above sloping terrain. *Tellus* **19**: 199–205.

Jiang XN, Lau N-C, Held IM, Ploshay JJ. 2007. Mechanisms of the Great Plains low-level jet as simulated in an AGCM. *J. Atmos. Sci.* **64**: 532–547.

Kotroni V, Lagouvardos K. 1993. Low-level jet streams associated with atmospheric cold fronts: Seven case studies selected from the FRONTS 87 experiment. *Geophys. Res. Lett.* **20**: 1371–1374.

Kraus H, Malcher J, Schaller E. 1985. A nocturnal low-level jet during PUKK. *Boundary-Layer Meteorol.* **31**: 187–195.

Lenderink G, Holtslag AAM. 2004. An updated length-scale formulation for turbulent mixing in clear and cloudy boundary layers. *Q. J. R. Meteorol. Soc.* **130**: 3405–3427.

Lundquist JK. 2003. Intermittent and elliptical inertial oscillations in the atmospheric boundary layer. *J. Atmos. Sci.* **60**: 2661–2673.

Shapiro A, Fedorovich E. 2009. Nocturnal low-level jet over a shallow slope. *Acta Geophys.* **57**: 950–980.

Shapiro A, Fedorovich E. 2010. Analytical description of a nocturnal low-level jet. *Q. J. R. Meteorol. Soc.* **136**: 1255–1262.

Singh MP, McNider RT, Lin JT. 1993. An analytical study of diurnal wind-structure variations in the boundary layer and the low-level nocturnal jet. *Boundary-Layer Meteorol.* **63**: 397–423.

Smedman A-S, Tjernström M, Högström U. 1993. Analysis of the turbulence structure of a marine low-level jet. *Boundary-Layer Meteorol.* **66**: 105–126.

Song J, Liao K, Coulter RL, Lesht BM. 2005. Climatology of the low-level jet at the Southern Great Plains atmospheric boundary layer experiments site. *J. Appl. Meteorol.* **44**: 1593–1606.

Stensrud DJ. 1996. Importance of low-level jets to climate: A review. *J. Climate* **9**: 1698–1711.

Stull RB. 1988. *An Introduction to Boundary Layer Meteorology*. Kluwer Academic Publishers: Dordrecht.

Tan Z-M, Farahani MM. 1998. An analytical study of the diurnal variations of the wind in a semi-geostrophic Ekman boundary layer model. *Boundary-Layer Meteorol.* **86**: 313–332.

Thorpe AJ, Guymer TH. 1977. The nocturnal jet. *Q. J. R. Meteorol. Soc.* **103**: 633–653.

Van den Brink L. 2010. '*Analysis of surface wind vectors in nights dominated by inertial oscillations.*' MSc thesis, Wageningen University, 43 pp. Available from Wageningen University, Wageningen, The Netherlands.

Van de Wiel BJH, Moene AF, Hartogensis OK, De Bruin HAR, Holtslag AAM. 2003. Intermittent turbulence in the stable boundary layer over land. Part III: A classification for observations during CASES-99. *J. Atmos. Sci.* **60**: 2509–2522.

Van de Wiel BJH, Moene AF, Steeneveld GJ, Baas P, Bosveld FC, Holtslag AAM. 2010. A conceptual view on inertial oscillations and nocturnal low-level jets. *J. Atmos. Sci.* **67**: 2679–2689.

Van Meijgaard E, Van Ulft LH, Van de Berg WJ, Bosveld FC, Van den Hurk BJJM, Lenderink G, Siebesma AP. 2008. '*The KNMI regional atmospheric climate model RACMO, version 2.1.*' KNMI Technical Report 302, 43 pp. Available from KNMI, Postbus 201, 3730AE, De Bilt, The Netherlands.

Van Ulden AP, Wieringa J. 1996. Atmospheric boundary layer research at Cabauw. *Boundary-Layer Meteorol.* **78**: 39–69.

Whiteman CD, Bian XD, Zhong SY. 1997. Low-level jet climatology from enhanced rawinsonde observations at a site in the Southern Great Plains. *J. Appl. Meteorol.* **36**: 1363–1376.

Wilczak JM, Cancillo ML, King CW. 1997. A wind profiler climatology of boundary layer structure above the boreal forest. *J. Geophys. Res.* **102**: 29083–29100.

